Science
AAAS

Supplementary Materials for

Time-resolved live-cell spectroscopy reveals EphA2 multimeric assembly

Xiaojun Shi *et al*.

Corresponding authors: Dimitar B. Nikolov, nikolovd@mskcc.org; Adam W. Smith, aw.smith@ttu.edu; Bingcheng Wang, bxw14@case.edu

Science **382**, 1042 (2023)
DOI: 10.1126/science.adg5314

The PDF file includes:

Other Supplementary Material for this manuscript includes the following:

Materials and Methods

Antibodies: Rabbit monoclonal Anti-EphA2 (Cell Signaling Technology, #6697S); Rabbit monoclonal Anti-Phospho-EphA2 (Ser897, Cell Signaling Technology, #6347S); Rabbit monoclonal Anti-Phospho-EphA/B (Miao et al., 2009 (*13*)); Rabbit monoclonal Anti-pan-Akt (Cell Signaling Technology, #4691); Rabbit monoclonal Anti-Phospho-Akt (Ser473, Cell Signaling Technology, #4060); Rabbit monoclonal Anti-Phospho-Erk1/2 (Thr202/Tyr204, Cell Signaling Technology, #4370); Rabbit polyclonal Anti-ERK1/ERK2 (R&D Systems, AF1576); Rabbit monoclonal Anti-Rab5 (Cell Signaling Technology, #3547); Rabbit monoclonal Anti-Rab 7 (Cell Signaling Technology, #9367); Goat Anti-Rabbit IgG-HRP (Santa Cruz Biotechnology, #sc-2301); Alexa Fluor 568 Goat Anit-Rabbit IgG (H+L, Thermo Fisher Scientific, #A11011); Cy3 Donkey Anti-Human IgG, Fcγ Fragment Specific (Jackson Immuno Research, #709-165-098).

Bacterial Strains: NEB 5-alpha Competent E. coli (New England BioLabs, #C2987); NEB Stable Competent E. coli (New England BioLabs, #C3040).

Recombinant Proteins: ephrinA1-Fc (Miao et al., NCB, 2000 (*12*)); Monomeric ephrinA1 (EMBO Report 2009 (*56*)).

Cell Lines: Human HEK-293 (ATCC, CRL-1573); *Cercopithecus aethiops* COS-7 (ATCC, CRL-1651); Human DU145 (ATCC, HTB-81); Human PC-3 (ATCC, CRL-1435); Mouse SCC728 (Shi et al., 2017 (*57*)); Mouse SCC748 (Shi et al., 2017 (*57*)); Mouse 283LM (this paper); Mouse GSC1816 (this paper); Human GSC827 (NIH-NCI, Lee et al., 2006 (*58*)); Human 293FT (Thermo Fisher Scientific, R70007); Human Phoenix-AMPHO (ATCC, CRL-3213).

Mouse Strains: C57BL/6J (Jackson Lab, 000664).

Oligonucleotides: EphA2 CRISPR KO, caccgCTTGGCGGTGATTGGCGGCG, aaacCGCCGCCAATCACCGCCAAGc;
EphA2 mutations: LBD: GAAGTTGGTGCTGTAGTTCAGGTCCGACTCGGC, GCCGAGTCGGACCTGAACTACAGCACCAACTTC;
Sushi 1: CAGTGGCCCGGGAAGGTGCATCAGAG, CTTCCCGGGCCACTGTGGCC;
Sushi 2: GGTCCTGCTGGAGTTCGTGACCGCCGCCGG, CCGGCGGCGGTCACGAACTCCAGCAGGACC;
FN2: CGCTCCACAAGGTAGCTGTTGGAGTCTCCC, CTACCTTGTGGAGCGCACCGAGGGTTTCTCC;
FN1: GGCCTCACACTCCCCGCATTCC, GAATGCGGGGAGTGTGAGGCC.

Recombinant DNA: human EPHA2 [aa 1-971 based on NM_004431.4] in Gateway donor vector with C-terminal mCherry (GeneCopoeia, CS-A0125-02), human EPHA2 [aa 1-971 based on NM_004431.4] in Gateway donor vector with C-terminal monomeric eGFP (GeneCopoeia, CS-A0125-05), human ephrinA1 (EFNA1) in Gateway donor vector with N-terminal mCherry (GeneCopoeia, CS-A0125-02), human ephrinA1 (EFNA1) in Gateway donor vector with N-terminal monomeric eGFP, (GeneCopoeia, CS-A0125-01), pLenti CMV Puro DEST (Addgene, Plasmid #17452), pLenti CMV Hygro DEST (Addgene, Plasmid #17454), LentiCRISPRv2 puro (Addgene, Plasmid #98290), pBABEpuro-gateway (Addgene, Plasmid #51070).

Commercial Assays: IncuCyte Scracth Wound Cell Migration Assay (Sartorius, #9600-0012, #4493); Costar Transwell 6.5 mm inserts, 8.0 μm pore size (Corning Incorporated, #3422).

Software and Algorithms: ImageJ (NIH), Matlab (MathWorks), Prism (GraphPad), DecayFit (FluorTools), FCCS data processing algorithms (this paper).

Establishment of glioma tumor cells (GSC1816)

Mouse mesenchymal glioblastoma cells 1861 which lack expression of Nf1 and Tp53 was maintained in 10% FBS containing DEMM high-glucose medium established as previously described (*51, 52, 59*).

Maintenance of Cell Lines

HEK-293, COS-7, DU145, 293FT, Phoenix, SCC748, SCC728, 283LM and GSC1816 cells were maintained on cell culture plates in Dulbecco's Modified Eagle Medium (DMEM) supplemented with 10% FBS and glutamine/penicillin/streptomycin at 37 ºC and 5% CO_2. The cell culture plates for maintaining SCC748 and SCC728 were coated with collagen. The establishment of SCC748 and SCC728 cells with EphA1/EphA2 knockout is reported in previous work. PC-3 cells were maintained on cell culture plates in RPMI Medium supplemented with 10% FBS and glutamine/penicillin/streptomycin at 37 ºC and 5% CO_2. GSC827 cells were maintained on cell culture plates in Neurobasal Medium supplemented with N2 supplement (Invitrogen, Cat#17502048), B27 supplement without Vitamin A (Invitrogen, Cat# 12587010), FGF, EGF, Geltrex and glutamine/penicillin/streptomycin at 37 oC and 5% CO_2. The GSC827 cells were kindly provided by Dr. Fine (NIH-NCI, Bethesda, MD, USA).

Plasmids

Human EphA2 cDNA (AA 1-971 based on NM_004431.4) with C-terminal GFP or mCherry tag were purchased from Origene in gateway donor vectors. Human EFNA1 cDNA (AA 1-70 based on NM_004428.2) with N-terminal GFP or mCherry tag were also purchased from GeneCopoeia in gateway donor vectors. The donor vectors were amplified with NEB 5α competent E. coli. (New England BioLabs, Cat #C2987). The donor vectors containing EphA2 constructs were shuttled into pLenti and pBabe gateway destination vectors with with puromycin or hygromycin selection marker using Gateway LR Clonase II (Thermo Fisher Scientific, Cat #56484) (GFP donor vector into puromycin destination vector, mCherry into hygromycin). The pLenti and pBabe gateway destination vectors were obtained from Addgene (Plasmid #17452, #17454 and #51070). The resulted pLenti and pBabe vectors containing EphA2 constructs were amplified with NEB stable competent E. coli. (New England BioLabs, Cat #C3040) and were used for Lenti/Retro virus production.

Mutations on EphA2 cDNA were carried out with site-directed mutagenesis on the gateway donor vectors by using Q5 High-Fidelity 2x Master Mix (New England BioLabs, Cat #M0492) and NEBuilder HiFi DNA Assembly kit (New England BioLabs, Cat #E2621). All the oligonucleotides used in site-directed mutagenesis were listed in the Key Resources Table. All plasmids generated in this study were sequenced to confirmed the right mutations.

Knock out of EphA2 from PC3 and 283LM cells were carried out with CRISPR-Cas9 system. The sgRNA targeting exon 8 of EphA2 gene was introduced into LentiCRISPRv2 puro (Addgene, Plasmid #98290) This was accomplished by digesting the empty vector with BsmBI in the presence of 10x NEBuffer 3.1 (NEB) and dephosphorylating the free ends with alkaline phosphatase (AP) (Roche Diagnostics). Oligos 5'-caccgCTTGGCGGTGATTGGCGGCG-3' and 5'-aaacCGCCGCCAATCACCGCCAAGc-3' were annealed and phosphorylated at the 5' ends using 10x T4 Ligation Buffer (NEB), and T4 PNK (NEB M0201S). The annealed portion was then ligated into the open lentiCRISPRv2 backbone using T4 DNA Ligase and Buffer (NEB).

Cell Transfection

The pLenti vectors containing both GFP and mCherry tagged EphA2 constructs were used for transient transfection of COS-7 cells using Lipofectamine 2000. The resulted COS-7 cells expressing dual-color EphA2 constructs were used in PIE-FCCS measurements.

Lenti- and Retro-virus Mediated Gene Transduction

The pBabe vectors containing EphA2 constructs were transfected into Phoenix retroviral packaging cells with Lipofectamine 2000. HEK-293, DU 145, PC-3, SCC728, SCC748, 283LM and GSC1816 cells were infected with retroviral-mediated gene transfer in the presence of 6mg/ml polybrene and selected in the presence of puromycin or hygromycin.

The pLenti vectors containing EphA2 constructs were transfected into 293FT cells with lentiviral packaging vectors with X-tremeGENE 9. GSC827 cells were infected with lentiviral-mediated gene transfer in the presence of 6 mg/ml polybrene and selected in the presence of puromycin or hygromycin.

The lentiCRISPRv2 vector containing sgRNA for knocking out EphA2 was transfected into 293FT cells with lentiviral packaging vectors with X-tremeGENE 9. PC3 cells were infected with lentiviral-mediated gene transfer in the presence of 6 mg/ml polybrene and selected in the presence of puromycin.

Live-cell Pulsed Interleaved Excitation – Fluorescence Cross-correlation Spectroscopy (PIE-FCCS)

Fluorescence cross-correlation spectroscopy measurements were performed on a customized Nikon Eclipse Ti inverted microscope (Nikon Corp., Tokyo, Japan) with home-built pulsed interleaved excitation and time-correlated single-photon detection. A continuum white light laser (9.7 MHz, SuperK NKT Photonics, Birkerod, Denmark) is used as excitation laser source. The source has an internal pulse picker that allows us to set the pulse rate. A wavelength splitter inside the emission box picks off a 488 nm ± 10 nm beam and directs the beam out with a second beam containing the rest of the white light. The second beam is sent through a 561 nm ± 20 nm dichroic mirror (z405/561rpc, Chroma Technology Cop., Bellows Falls, VT) to separate out the 561 nm light, the rest of the white light is directed to a beam dump. The 488 and 561 nm beams pass through narrow-band excitation filters (488: LL01-488-12.5; 561: LL02-561-12.5, respectively; Semrock, Rochester, NY) before being coupled into single-mode optical fibers (488: QPMJ-3AF3U-488-3.5/125-3AS-18-1-SP; 561: QPMJ-3AF3U-488-3.5/125-3AS-3-1-SP; OZ Optics, Ottawa, Ontario). The 488 nm beam passes through a 3 m fiber while the 561 nm beam passes through an 18 m fiber. The 15 m-length difference of the two fibers introduces a 50 ns delay between the two pulse trains which is used for pulsed interleaved excitation (PIE). The beams exit the fibers and are collimated with infinity corrected objective lenses (L-10x, Newport, Irvine, CA). Continuously variable ND filters are placed after the lenses so that selected laser powers can be set independently for each one of the beams. The two beams are directed to a 503 nm cutoff dichroic beamsplitter (LM01-503-25, Semrock, Rochester, NY) to achieve spatial overlap before being sent into the optical path of the microscope. A customized TIRF filter cube (91032, Chroma Technology Corp., Bellows Falls, VT) with a two-color dichroic mirror and laser blocking filer (zt488/561rpc and zet488/561m, Chroma Technology Corp., Bellows Falls, VT) is used to allow the beams being fed to the objective. A 100X TIRF (oil) objective, NA 1.49, (Nikon Corp., Tokyo, Japan) was used to focus the excitation beams on the sample and collect the emitted photons. For time-correlated single photon detection, the emitted photons pass through a 50 μm pinhole placed at the output port of the microscope to achieve confocal detection. The beam is collimated with a 100 mm focal length achromatic lens (AC254-100-A-ML, Thorlabs Inc., Newton, NJ) and then split into two beams with a 560 nm long-pass beamsplitter (FF560-FDi01-25X36, Semrock, Rochester, NY). The beams are directed through a 520/44 nm emission filter (FF01-520/44-25, Semrock, Rochester, NY) and a 612/69 nm emission filter (FF01-621/69-25, Semrock , Rochester, NY) to obtain a green (520 nm) and a red (612 nm) emission beam, respectively. Each beam is focused to a single photon avalanche diode (SPAD) detector (Micro Photon Devices, Bolzano,

Italy) with a time-resolution of 30 ps and 50 μm^2 active area, 25 dark counts per second. Signals collected by the detectors are recorded with a four-channel-routed time-correlated single photon counting (TCSPC) card (Picoharp 300, PicoQuant, Berlin, Germany) which is synchronized with the white light laser source. Data recorded by TCSPC card is input to a computer for correlation with a home-written Matlab script.

In live cell PIE-FCCS measurements, cells were plated on MatTek glass bottom culture dish. PIE-FCCS measurements were performed on live cells situated in Opi-MEM at 37 oC. For stimulation, cells were incubated in 1 μg/ml ligand for 20 min prior to measurements. The laser beams were set at 300 nW (488 nm) and 800 nW (561 nm) and were focused at flat peripheral membrane area of the cell. Five set of 10 s measurements were taken on one cell and were averaged into one data point. Details of data processing is described in the following section.

Live-cell Fluorescence Anisotropy

The TIRF-based fluorescent anisotropy analysis was done using a modified TIRF system (Intelligent Imaging Innovations, Inc, Denver, CO, USA) equipped with a W-view Gemini system (Hamamatsu photonics, Bridgewater, NJ). In specific, excitation polarization was achieved through a fiber switcher (Intelligent Imaging Innovations, Inc, Denver, CO, USA) where only P-Polarized 488nm excitation was illuminating the cell membrane. Fluorescent emission passed through a 532nm polarized beam splitter (Thorlabs, Inc, Newton, NJ) that separates the s- and p-emission into two separate parts of the camera chip. The microscope system was equipped with a Prime 95B Scientific CMOS camera (Photometrics), maintained at -10 °C.

Immuno-fluorescence Imaging

GSC827 cells were plated on coverslips in 24-well cell culture dish for ephrinA1-Fc (EA1-Fc) binding assay. Cells were kept on ice while 3 μg/ml of EA1-Fc were added. After 10 min incubation, cells were fixed with 4 % PFA and washed with PBS. The EA1-Fc bound to cell surface were stained with Cy3 conjugated donkey anti-human IgG with Fc fragment specificity for visualization. The stained cells were mounted with DAPI staining and imaged with Leica DMi8 Epi-Fluorescence Microscope.

HEK293 and GSC827 cells were plated on coverslips in 24-well cell culture dish for investigation of the cell membrane localization of EphA2. Cells were stimulated with 3 μg/ml of EA1-Fc for 1 h. Unstimulated and stimulated cells were fixed with 4 % PFA and then mounted with DAPI staining. The mounted cells were imaged with Leica DMi8 Epi-Fluorescence Microscope.

GSC827 cells were plated on coverslips in 24-well cell culture dish for endosome immune-fluorescence imaging. Cells were stimulated with 3 μg/ml EA1-Fc for 15 min and 1 h. Unstimulated and stimulated cells were fixed with 4 % PFA and then permeabilized with Triton X-100 for 5 min. The fixed cells were blocked with 3 % BSA overnight and then incubated with either rabbit monoclonal anti-Rab 5 or Rab 7 overnight. After washing off the primary antibodies, Alexa Fluor 568 goat anti-rabbit IgG were added and incubated for 1 h. The cells were then mounted with DAPI staining and imaged with Leica DM5500Q Confocal Microscope.

Ligand Stimulation, Whole Cell Extraction and Western Blot Analysis

200,000 cells were plated on 6-well cell culture dish and incubated overnight. The cells were stimulated with 3 μg/ml ephrinA1-Fc or monomeric ephrinA1. At indicated times, cells were lysed in modified RIPA buffer (20mM Tris, pH 7.4, 120 mM NaCl, 1 % Triton X-100, 0.5 % sodium deoxycholate, 0.1 % SDS, 10 % glycerol, 5 mM EDTA, 50 mM NaF, 0.5 mM Na3VO4, phosphatase inhibitor cocktail, and protease inhibitors, including 1 mM phenylmethylsulphonyl fluoride, and 2 mg/ml each of aprotinin and leupeptin). Lysate were centrifugated at 13,000 g for

10 min at 4 ºC, and either analyzed immediately or stored at -80 ºC. Whole cell lysates were resolved by Bolt 4-12 % Bis-Tris Plus gel (Invitrogen, Cat#NW04125BOX) and electrotransferred onto polyvinylidene difluoride membranes (Millipore, Cat#IPVH00010), which were then blotted with the indicated antibodies. Antibodies used include rabbit monoclonal anti-EphA2 (Cell Signaling Technology, Cat #6697S), rabbit monoclonal anti-Phospho-EphA2 Ser897 (Cell Signaling Technology, Cat #6347S) and rabbit monoclonal anti-EphA/B which was custom-raised against the phosphorylated di-tyrosine motif in the conserved juxtamembrane motif of Eph receptors. Same membrane was used for blotting with different antibodies after stripping the previous blot.

Live-cell Microscopy

HEK293, PC-3 cells were plated on 24-well cell culture dish. During imaging assay, cells were kept in INU WSKM on-stage incubation chamber (Tokat Hit) at 37 ºC and 5% CO_2. 3 μg/ml EA1-Fc were added to stimulate cells. Bright field images were taken on Leica DMi8 Microscope with 1 min interval.

SCC728 cells were plated on MatTek glass bottom culture dish. During imaging assay, cells were kept in on-stage incubation chamber at 37 oC and 5% CO2. 3 μg/ml EA1-Fc were added to stimulate cells. Epi-fluorescence images were taken on Nikon Eclipse Ti Microscope with 1 min interval.

Cell Migration

Costar Transwell inserts (8.0 μm pore size) were coated with collagen. 150 μL 500,000 cell/ml HEK293 suspension in 0.5 % FBS/DMEM were added in the inserts. The inserts were drop into 550 μL 20 % FBS/DMEM supplemented with 20 μg/ml EGF and 10 μg/ml FGF. After 5 h incubation, the inserts were moved into 4 % PFA solution for cell fixation. After fixing, the cells were stained with 0.1 % Crystal Violet in 20 % methanol solution. The cells on the top part of the membrane were gently swabbed off with Q-tips. The cells on the bottom part of the membrane were imaged on Leica DMi8 microscope. The number of cells from one image was counted and 5 random areas on the same membrane were used for averaging.

96-Well ImageLock Microplate (Sartorius, Cat# 4379) were coated with collagen. 18,000 SCC728 cells and 20,000 283LM cells were plated to each well and incubated overnight. IncuCyte WoundMaker (Sartorius, Cat# 4493) was used to create scratch wounds. The cells were incubated and imaged in IncuCyte S3 for 24 h with 1 h interval. 12 wounds were used for each group for averaging.

Tumor Cell Injections

Injections were performed on a stereotactic fixation device (Stoetling). Mice were anaesthetized with intraperitoneal (IP) injections of ketamine (0.1 mg/g) (McKesson, 494158) and xylazine (0.01 mg/g) (Akorn) prior to shaving the head with battery-powered clippers. A local injection of 50 μl of marcaine (McKesson, 57199) was delivered subcutaneously in the scalp for pre-surgical analgesia. Mice were then loaded onto the stereotactic fixation device and a small caudal incision was made on the scalp to the right of the midline with a surgical scalpel. The skull was then blotted dry with sterile cotton tipped applicators and a burr hole was made in the skull with a surgical drill. For the injections, 75,000 tumor cells were injected into the subventricular zone at AP-0.0mm and right-0.5mm from bregma; depth-1.5mm from the dural surface. The scalp was sealed with GLUture (WPI, 503763) and sterilized with iodine before placing the mice on a heating pad until cessation of anesthesia. Mice were then treated with 50 μl of buprenorphine (McKesson, 1013922) subcutaneously at the site of incision prior to returning to their cage as well as once more within 24 hours of the surgery. Mice were continually monitored for signs of tumor

burden and were sacrificed upon observation of endpoint symptoms including head tilt, lethargy, seizures, and excessive weight loss.

At endpoint, mice were sacrificed via ketamine overdose and perfused with sterile Ringer's solution (Sigma-Aldrich, 96724-100TAB). The brain was extracted and transferred to 10% neutral-buffered formalin (Sigma-Aldrich, HT501128) for 72 hours. Fixed tissues were embedded in paraffin and 5 μm formalin-fixed paraffin embedded (FFPE) sections were cut on a microtome (Leica). The sections were deparaffinized in histo-clear (Fisher Scientific, 50-899-90147) and were passed through graded alcohols prior to H&E staining for tumor verification.

All mouse experimental procedures were approved by the Institutional Animal Care and Use Committee (IACUC) of Emory University (Protocol #2017-00633 - PI Hambardzumyan Dolores)

Brain Imaging and Histology

Mouse brains were removed and fixed in 10 % formalin solution. Whole brain samples were imaged with Leica S6D microscope. Fixed brain samples were embedded in paraffin. Sections (5 mm) were cut and stained with hematoxylin and eosin (H&E). Slices are sealed with neutral resin after clearing steps and imaged with Nikon Eclipse E600 microscope.

TCGA Data Analysis

RNA-sequencing based EPHA2 gene expression in GBM tumors and normal samples, quantified as Fragments Per Kilobase of transcript per Million mapped reads (FPKM), was obtained from The Cancer Genome Atlas Pan-Cancer analysis project (*60*), followed by addition of pseudo-counts and Log2 transformation. Expression-based molecular subtyping of the GBMs into Proneural, Mesenchymal and Classical subtypes was performed as outlined (*61*). The statistical significance of EPHA2 expression differences across molecular subtypes was evaluated using a two-sided Student's t-test assuming unequalvariances.

Analysis of Live-cell PIE-FCCS data

In fluorescence correlation spectroscopy (FCS), temporal fluctuations in the fluorescence signal are auto correlated with respect to a lag time, τ. The normalized autocorrelation function (ACF) is defined by

$$G(\tau) = \frac{\langle F(t+\tau)F(t)\rangle}{\langle F(t)\rangle^2} \quad \text{(eq. 1)}$$

where ⟨ ⟩ stands for time average and F(t) is fluorescence intensity at time t. The plot of the ACF versus lag time produces a curve that describes the mobility and concentration of the ensemble during the acquisition time within the Rayleigh-limited confocal volume. Dual color excitation is used in FCCS to quantify interactions between two differently labeled species. The cross-correlation of the two detection channels reveals the population of co-diffusing species. From the relative populations of all the species present in a sample, the degree of oligomerization can be determined.

In cross-correlation spectroscopy, fluorescence fluctuations in each detection channel are cross-correlated (CCF). In our experiment, the two channels are labeled red and green and the CCF becomes:

$$G_X(\tau) = \frac{\langle F_r(t+\tau)\cdot F_g(t)\rangle}{\langle F_r(t)\rangle\langle F_g(t)\rangle} \quad \text{(eq. 2)}$$

The amplitude of the correlation function is directly related to the relative population, N, of each species of diffusing fluorophore. The amplitude in each channel is then

$$G_r(0) = \frac{1}{\langle N_r + N_{rg}\rangle} \quad \text{(eq. 3)}$$

$$G_g(0) = \frac{1}{\langle N_g + N_{rg}\rangle} \quad \text{(eq. 4)}$$

$$G_X(0) = \frac{N_{rg}}{\langle N_g + N_{rg}\rangle\langle N_r + N_{rg}\rangle} = G_r(0) * G_g(0) * N_{rg} \quad \text{(eq. 5)}$$

The correlation curve in the confocal volume is related to the Brownian dynamics through the dwell time, τ_D.

$$G(\tau) = G(0)\frac{1}{\left(1+\frac{\tau}{\tau_D}\right)} \quad \text{(eq. 6)}$$

in which

$$\tau_D = \frac{\omega_0^2}{4D} \quad \text{(eq. 7)}$$

where ω_0 is the lateral distance where the excitation intensity reaches $1/e^2$ of its value from the center of the confocal volume and D is the diffusion coefficient of the fluorescent molecule (typically reported in $\mu m^2/s$). In our setup, ω_0 of 488 nm and 561 nm focal beams are 0.21 μm and 0.23 μm, respectively.

The cross-correlation value reflects the fraction of bound molecules, f_c, is determined by a ratio of the relative populations

$$f_c = \frac{N_{rg}}{\min\left[(N_r + N_{rg}),(N_g + N_{rg})\right]} \quad \text{(eq. 8)}$$

The cross-correlation value (fc) ranges from 0 to 1, indicating zero co-diffusion to complete co-diffusion.

Fluorescent proteins, such as GFP and mCherry, have a long triplet state lifetime. Hence, a modified Brownian model with triplet relaxation was used to fit the correlation curves:

$$G(\tau) = \frac{1}{\langle N\rangle}\frac{1-F+Fe^{-\tau/\tau_T}}{1-F}\frac{1}{1+\tau/\tau_D} \quad \text{(eq. 9)}$$

where F is the fraction of molecules in the triplet state, τ_T is the triplet relaxation time.

The time-tagged photons from each 10 s measurement were recorded and transformed into ACFs and CCF according to equation (1) and (2). The correlation curves from five repetitive measurements on one cell were averaged and fitted to the modified Brownian model with triplet relaxation (equation (9)) to yield τ_D and N. The cross-correlation values (f_c) were calculated based on N according to equation (8). The apparent diffusion coefficients were calculated based on τ_D according to equation (7). The cross-correlation values (f_c) were summarized in box-whisker plots. The boxes represent third quartile, median and first quartile and the whiskers indicate 10-90th percentile. The total cell number used were reported on top of the box-whisker plots. The apparent diffusion coefficients are summarized in bar graph to report the mean. The error bars represent the SEM values.

Analysis of Live-cell Fluorescence Anisotropy Data

Cells were maintained at 37°C and 5% CO_2 using a stage incubator (Oko-Lab, Pozzuoli, NA, Italy) and imaged alive on a MatTek dish (MatTek Co, MA) coated with rat tail collagen (ThermoFisher, PA, USA).

The analysis of fluorescent anisotropy was determined as described by previous published work (*62,63*). In specific, the fluorescent anisotropy of the image was defined as:

$$r = \frac{I_{\parallel} - GI_{\perp}}{I_{\parallel} + 2GI_{\perp}} \quad \text{(eq. 10)}$$

Where the fluorescent intensity of S-emission and P emission were background corrected using a collagen-coated MatTek dish. The G value of the system was determined using both 0.1μM GFP (ThermoFisher Scientific, PA) solutions and (0.01mM) Rhodamine-6-G solutions (TheromoFisher Scientific, OR) at 37°C, according to the previous description (*62*).

Analysis of Fluorescence Lifetime Data

The photons form PIE-FCCS measurements were recorded and binned into fluorescence lifetime histogram. The histograms from five 10 s measurements on one cell were averaged. The averaged histogram was deconvoluted with an instrument response function and fitted to a single exponential decay to yield the fluorescence lifetime of GFP. The fluorescence lifetimes (τ_{fl}) were used to calculate the average FRET efficiency,

$$E_{FRET} = 100\% \times \left(1 - \frac{\tau_{fl}}{\tau_0}\right) \quad \text{(eq. 11)}$$

where τ_0 is fluorescence lifetime of the monomeric control, Myr-FP, with only the GFP version expressed in cell. The lifetimes of different controls were shown in Figure S1.

Molecular modeling and structure refinement

We refined an all-atom structure of the EphA2 extracellular domain (ECD) using Rosetta (*69*) starting from a crystallographic pose of the EphA2 ECD dimer (PDB ID 3FL7). Sequence gaps in the PDB structure were filled using RosettaCM (*65*) and refined using the Rosetta FastRelax application in the REF2015 score function (*66*) with constraints on input backbone and sidechain atom coordinates. Subsequently, we created individual structures of monomeric domains of the EphA2 ECD, including the ligand-binding domain (LBD), Sushi domain, and fibronectin 1 (FN1) and FN2 domains. Each of these structures was refined with Rosetta FastRelax using dualspace minimization in the Cartesian REF2015 score function again with constraints to starting coordinates. Afterward, constraints were removed, and each domain was optimized with FastRelax in Cartesian space with an extended 9.0 Å electrostatic cutoff. A total of 50 structures were generated for each individual domain and the best scoring structure from each was used for subsequent model building and analysis. We used the Rosetta CartesianDDG application (*67*) to introduce the putative dimer-disrupting mutations into the best scoring model of the individual domains. Specifically, the following mutations were made: (i) LBD D129N/G131S, (ii) Sushi L223R/L254R/L255R, (iii) and FN2 N483L/R485E.

Molecular dynamics (MD) simulations

We performed MD simulations on our refined isolated EphA2 ECD subdomains. All of our systems were parameterized using Leap in AmberTools22 (AMBER 2020, UCSF). We employed the ff14SB force field (*68*) for proteins alongside the TIP3P water model and neutralized with Joung–Cheatham monovalent ions (*69*) and buffered on all sides with 12.0 Å solvent. Simulations were performed with Amber22 using pmemd.cuda. Hydrogen mass repartitioning was performed on solute atoms to allow a simulation timestep of 4.0 fs (*70*).

Minimization was performed in three stages: (i) 5000 cycles of steepest descent followed by 5000 steps of conjugate gradient descent (CGD) while protein atoms were restrained with a force constant of 5.0 kcal·mol^{-1}·Å^{-2}; (ii) 5000 cycles of steepest descent followed by 5000 steps CGD minimization while buffer atoms were restrained with a force constant of 5.0 kcal·mol^{-1}·Å^{-2}; (iii)1000 steps steepest descent followed by 9000 steps of CGD minimization with no restraints.

Following minimization, covalent bonds to hydrogen atoms were constrained with the SHAKE algorithm (*71*). Periodic boundary conditions were imposed on the system and the Particle Mesh Ewald (PME) approximation was employed for long-range interactions beyond 9.0 Å. Temperature was controlled using Langevin dynamics with a collision frequency of 5 ps^{-1} during heating and 2 ps^{-1} in production simulations. A unique random seed was used for each Langevin dynamics simulation. Systems were heated from 10K to 100 K in the canonical (NVT; constant number of particles, temperature, and volume) ensemble over 500 ps with a 0.1 fs timestep. Subsequently, systems were heated in the NPT (isothermal-isobaric) ensemble at 1.0 bar with isotropic position scaling from 100 to 310 K over 1000 ps and a 1.0 fs timestep. Pressures were maintained with a Monte Carlo barostat.

Production simulations were run in the NPT ensemble at 1.0 bar and 310 K with an integration timestep of 4.0 fs. A total of five independent trajectories for each of the wild-type and mutant systems were run for 2.0 μs each for a total simulation time of 60.0 μs. Simulation trajectory frames containing solute atoms were collected every 10 ps.

MD simulation analysis, including root-mean-square fluctuations (RMSF) and root-mean-square deviation (RMSD), were performed with CPPTRAJ (*72*). RMSF and RMSD calculations were performed with respect to backbone heavy atoms (N, CA, C, and O).

Statistical Analysis

Statistical analyses were performed with GraphPad Prism 8 software, using the unpaired one-way ANOVA test with Tukey's multiple comparison and two-tailed T test. All statistical tests, comparisons, and sample sizes are included in the Figures and Figure Legends. In all cases, ****$p < 0.0001$, ***$p < 0.0002$, **$p < 0.002$, *$p<0.02$, ns = not statistically significant, $p > 0.05$.

Data and Code Availability

The accession code for the EphA2 structure reported in this paper is PDB: 3FL7 (Protein Data Base). All other algorithms and data supporting the findings of this study are included in the main text or available from the authors upon reasonable request.

Supplementary Text

The mutations at the EphA2 head-to-head and head-to-tail interfaces may destabilize the monomeric protein structure, and thus the effects that we are observing could hypothetically be due to domain destabilization rather than dimer disruption. To address this concern and validate our EphA2 mutants, we performed 60.0 μs of aggregate molecular dynamics (MD) simulations on the isolated the domains of the EphA2 extracellular region. Specifically, we performed 5 independent trajectories of 2.0 μs each for the LBD wild-type, LBD D129/G131S, Sushi wild-type, Sushi L223R/L254R/L255R, FN2 wild-type, and FN2 N483L/R485E mutants. We analyzed our results by calculating the root-mean-square fluctuation (RMSF) of each residue and the time-dependent root-mean-square deviation (RMSD) of each protein from their crystallographically determined structures. In destabilizing mutants, we expect to see increased RMSF due to local strain and/or structural rearrangement. Further, in a scenario in which a mutant transition to a new stable conformation, we would expect to see a sharp rise in RMSD after the initial equilibration period followed by a plateau indicating stability in a new conformational state.

We observe in our MD simulations that the per-residue RMSF in each of our mutants is equivalent to or lower than the per-residue RMSF of the corresponding wild-type structure (**Fig. S2B,** top). Indeed, the hydrophobic-to-hydrophilic mutations in the Sushi domain may stabilize the monomeric structure by removing poorly soluble hydrophobic residues from exposure to bulk solvent. In addition, the time-dependent RMSD calculations do not suggest transitions to any alternative conformational statesc (**Fig. S2B,** bottom). The Sushi domain, both wild-type and mutant proteins, displays the largest time-dependent RMSD variance among the three ECD domains, which is unsurprising given its extensive loop composition. Overall, we conclude that the mutations are unlikely to destabilize the tertiary structure of the domains or cause transitions to alternative folded states, and that it is more likely that the mutations disrupt the dimerization interface.

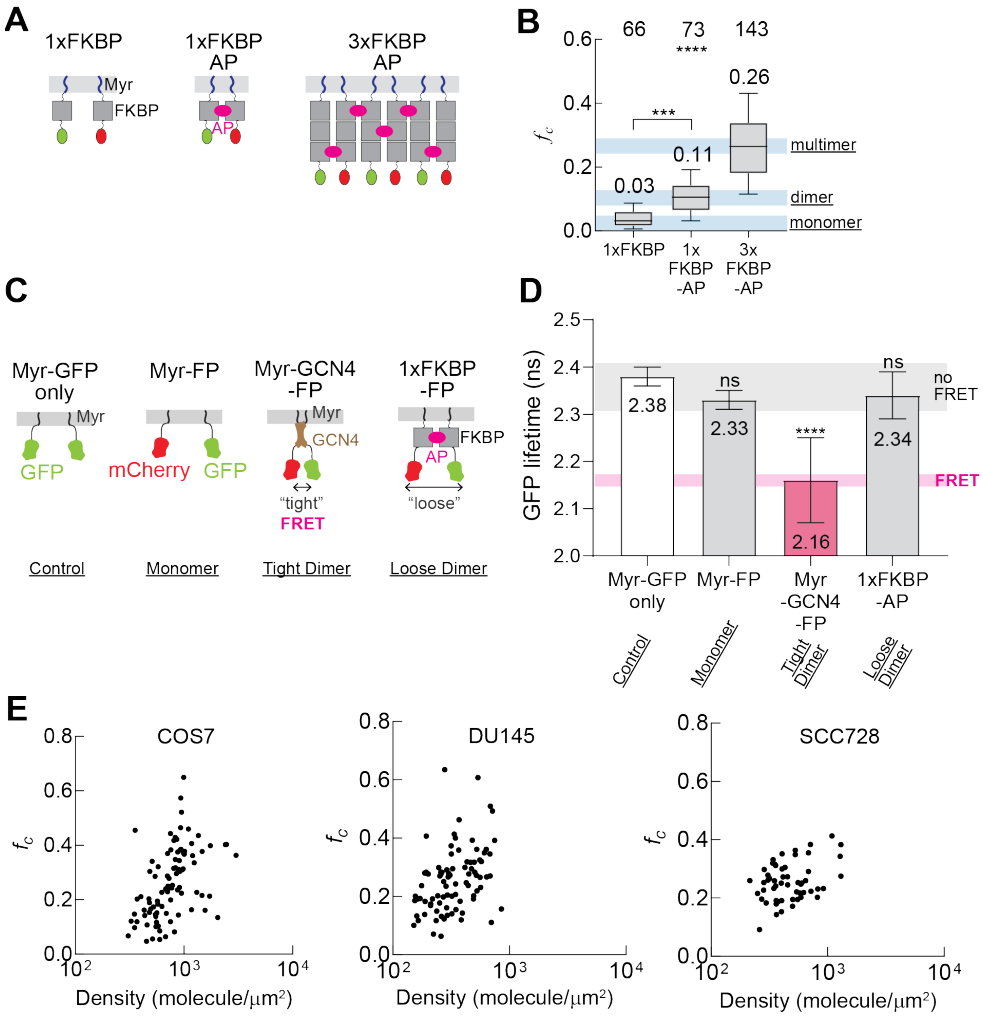
A
1xFKBP
1xFKBP AP
3xFKBP AP
Myr
FKBP
AP
B
66
73
143
****
***
0.26
0.11
0.03
multimer
dimer
monomer
1xFKBP
1x FKBP -AP
3x FKBP -AP
C
Myr-GFP only
Myr-FP
Myr-GCN4 -FP
1xFKBP -FP
GFP
mCherry
GCN4
"tight"
FRET
"loose"
Control
Monomer
Tight Dimer
Loose Dimer
D
GFP lifetime (ns)
2.38
ns
2.33
****
2.16
ns
2.34
no FRET
FRET
Myr-GFP only
Myr-FP
Myr -GCN4 -FP
1xFKBP -AP
E
COS7
DU145
SCC728
Density (molecule/μm²)

Figure S1 in supporting of Figure 1.
A) Cartoon depiction of the FKBP control constructs. AP20187 (AP) is used to induce dimerization of FKBP domain. **B)** Cross-correlation values (f_c) of the FKBP FCCS control constructs reported previously. **C)** Cartoon depiction of control constructs that have different distance between the fluorescent protein labels. The GCN4 coiled-coil induces tight dimerization with a space ~3 nm while the bulky FKBP protein induce dimer with loose space between the GFP and mCherry labels. **D)** Fluorescence lifetime of GFP of different control constructs. The lifetime are summarized in bar graph to report the mean. The error bars represent the SEM values. Only the tight dimer control Myr-GCN4-FP shows significantly shorter lifetime, indicating FRET from GFP to mCherry. Very little decrease of GFP lifetime is observed in 1xFKBP-FP suggesting negligible degree of FRET. **E)** Cross-correlation values (f_c) of ligand-free EphA2 plotted against molecular density.

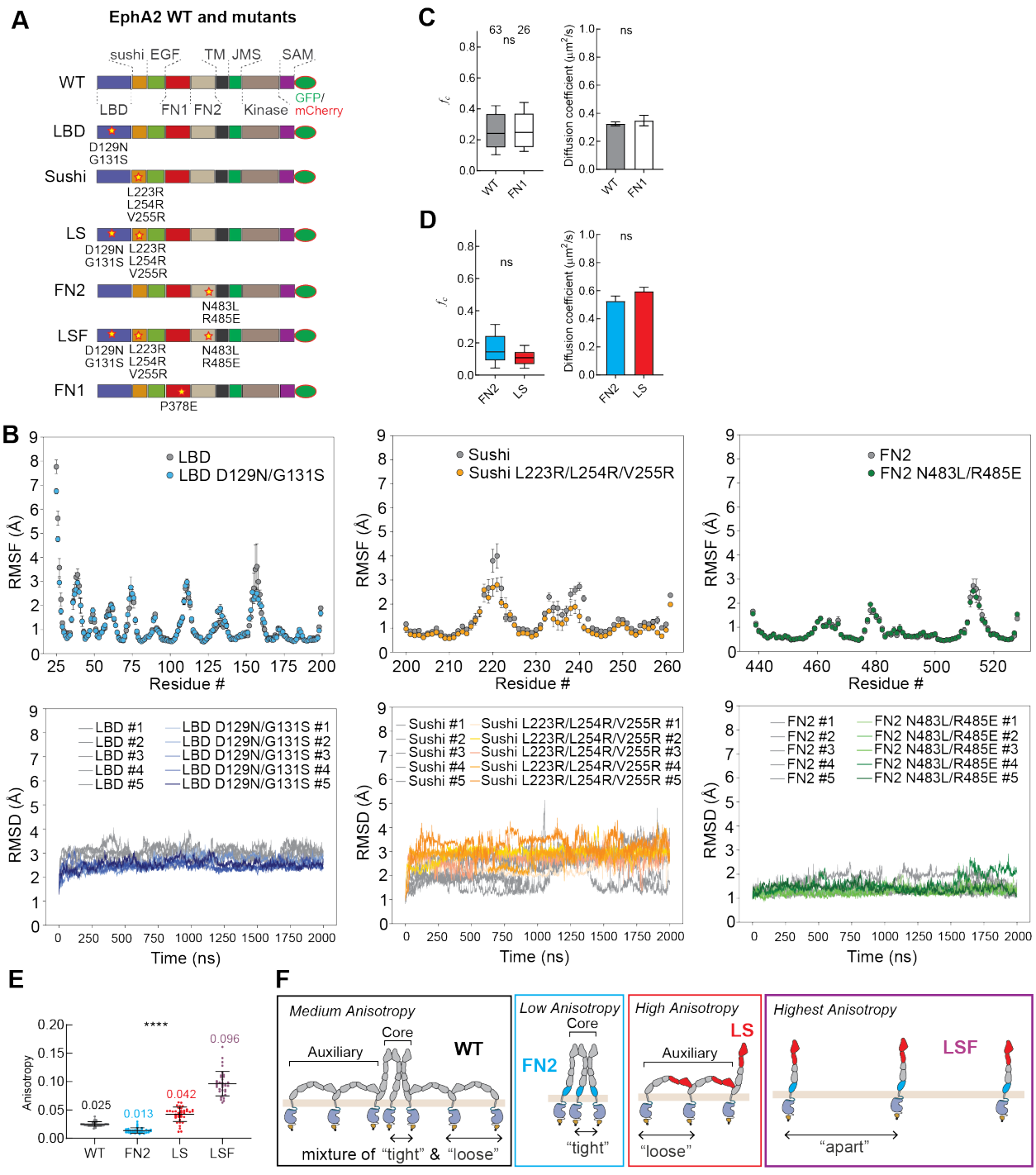
A
EphA2 WT and mutants
sushi EGF TM JMS SAM
WT
LBD FN1 FN2 Kinase
GFP/ mCherry
LBD
D129N G131S
Sushi
L223R L254R V255R
LS
D129N G131S L223R L254R V255R
FN2
N483L R485E
LSF
D129N G131S L223R L254R V255R
N483L R485E
FN1
P378E
C
63 26
ns
f_c
Diffusion coefficient (μm²/s)
WT FN1
D
FN2 LS
B
LBD
LBD D129N/G131S
Sushi
Sushi L223R/L254R/V255R
FN2
FN2 N483L/R485E
RMSF (Å)
Residue #
RMSD (Å)
Time (ns)
LBD #1 LBD #2 LBD #3 LBD #4 LBD #5
LBD D129N/G131S #1 LBD D129N/G131S #2 LBD D129N/G131S #3 LBD D129N/G131S #4 LBD D129N/G131S #5
Sushi #1 Sushi #2 Sushi #3 Sushi #4 Sushi #5
Sushi L223R/L254R/V255R #1 Sushi L223R/L254R/V255R #2 Sushi L223R/L254R/V255R #3 Sushi L223R/L254R/V255R #4 Sushi L223R/L254R/V255R #5
FN2 #1 FN2 #2 FN2 #3 FN2 #4 FN2 #5
FN2 N483L/R485E #1 FN2 N483L/R485E #2 FN2 N483L/R485E #3 FN2 N483L/R485E #4 FN2 N483L/R485E #5
E
Anisotropy
****
0.025 0.013 0.042 0.096
WT FN2 LS LSF
F
Medium Anisotropy
Auxiliary
Core
WT
mixture of "tight" & "loose"
Low Anisotropy
Core
FN2
"tight"
High Anisotropy
Auxiliary
LS
"loose"
Highest Anisotropy
LSF
"apart"

Figure S2 in supporting of Figure 2.
A) Diagram of EphA2 constructs used in this study. **B)** Per-residue averaged root-mean-square fluctuations (RMSF) and time-dependent root-mean-square deviation (RMSD) of all atom molecular dynamics (MD) simulation trajectories of the isolated EphA2 LBD, Sushi, and FN2 domain. For each protein (wild-type or mutant), we ran 5 independent simulations of 2.0 μs each for a total simulation time of 60.0 μs. The RMSF values are averaged across the 5 independent trajectories. RMSF error bars indicate the standard error of the mean across the 5 independent trajectories. **C)** Cross-correlation values (left) and diffusion coefficients (right) of WT EphA2 and FN1 mutant. The boxes represent third quartile, median and first quartile and the whiskers indicate 10-90th percentile. The total cell number used were reported on top of the box-whisker plots. The apparent diffusion coefficients are summarized in bar graph to report the mean and SEM values. (Two tail T test, ns: not significant) **D)** Cross-correlation values (left) and diffusion coefficients (right) of ligand-free FN2 and LS. FN2 and LS are in the similar oligomerization state. **E)** Anisotropy of EphA2-GFP constructs. Median value and SEM are shown. (One-way ANOVA test. ****: $p < 0.0001$) **F)** Cartoons illustrating the different intracellular proximity caused by different extracellular contacts.

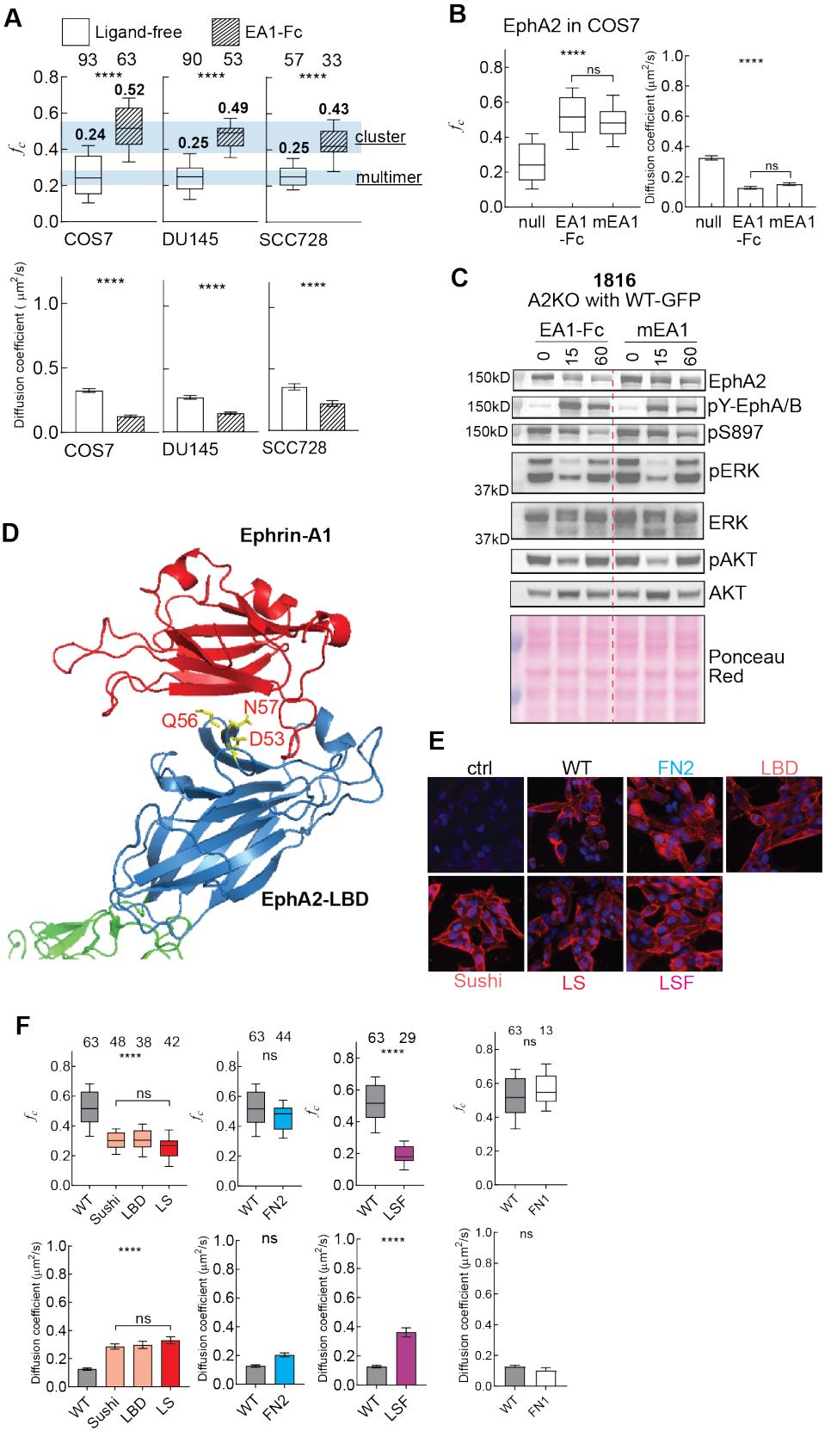
A
Ligand-free
EA1-Fc
93 63
90 53
57 33
****
0.52
0.49
0.43
0.24
0.25
0.25
cluster
multimer
COS7
DU145
SCC728
Diffusion coefficient (μm²/s)
B
EphA2 in COS7
ns
null
EA1 -Fc
mEA1
C
1816
A2KO with WT-GFP
EA1-Fc
mEA1
0
15
60
150kD
EphA2
pY-EphA/B
pS897
37kD
pERK
ERK
pAKT
AKT
Ponceau Red
D
Ephrin-A1
N57
Q56
D53
EphA2-LBD
E
ctrl
WT
FN2
LBD
Sushi
LS
LSF
F
63 48 38 42
63 44
63 29
63 13
WT
Sushi
LBD
LS
FN2
LSF
FN1

Figure S3 in supporting of Figure 2.
A) Cross-correlation values (top) and diffusion coefficients (bottom) of ligand-free and ephrin-A1-Fc (EA-Fc) stimulated EphA2 in the plasma membranes of three cell types. **B)** Cross-correlation values (top) and diffusion coefficients (bottom) of monomeric ephrinA1 (mEA1) or dimeric ephrin-A1-Fc (EA1-Fc) WT EphA2. The two different version of ligands induce EphA2 clusters with similar size. **C)** EphA2-WT are expressed in 1816 EphA2KO cells. Cells are stimulated with 3 μg/mL EA1-Fc or mEA1 for 15 min and 60 min, and lysed. Whole-cell lysates are subjected to immunoblot with the indicated antibodies. **D)** Structure of ephrinA1 binding with LBD of EphA2. The residues involved in LBD-FN2 head-tail interaction are shown in yellow sticks and labeled. This LBD-FN2 interface locates close to the ligand-binding pocket on LBD and is blocked by ligand-binding. **E)** WT and mutant EphA2 bind to EA1-Fc ligand equally well on GSC827 cells. Cell were incubated with 10 nM EA1-Fc for 30 minutes on ice. Bound EA1-Fc was visualized with red fluorescent anti-Fc antibodies. **F)** Cross-correlation values (top) and diffusion coefficients (bottom) of EA1-Fc stimulated EphA2 constructs (Sushi, LBD and LS) with disruption at HH contact, FN2 with disruption at HT contact and LSF with disruption at both HH and HT contacts. Obvious difference in the cross-correlation values is observed between EA1-Fc stimulation and mEA1 stimulation shown in Figure 2, especially those of EA1-Fc stimulated LSF are close to dimer control, indicating that EA1-Fc stimulation causes bias in oligomerization states. (Two tail T test and one-way ANOVA test. ****: $p < 0.0001$; ns: not significant)

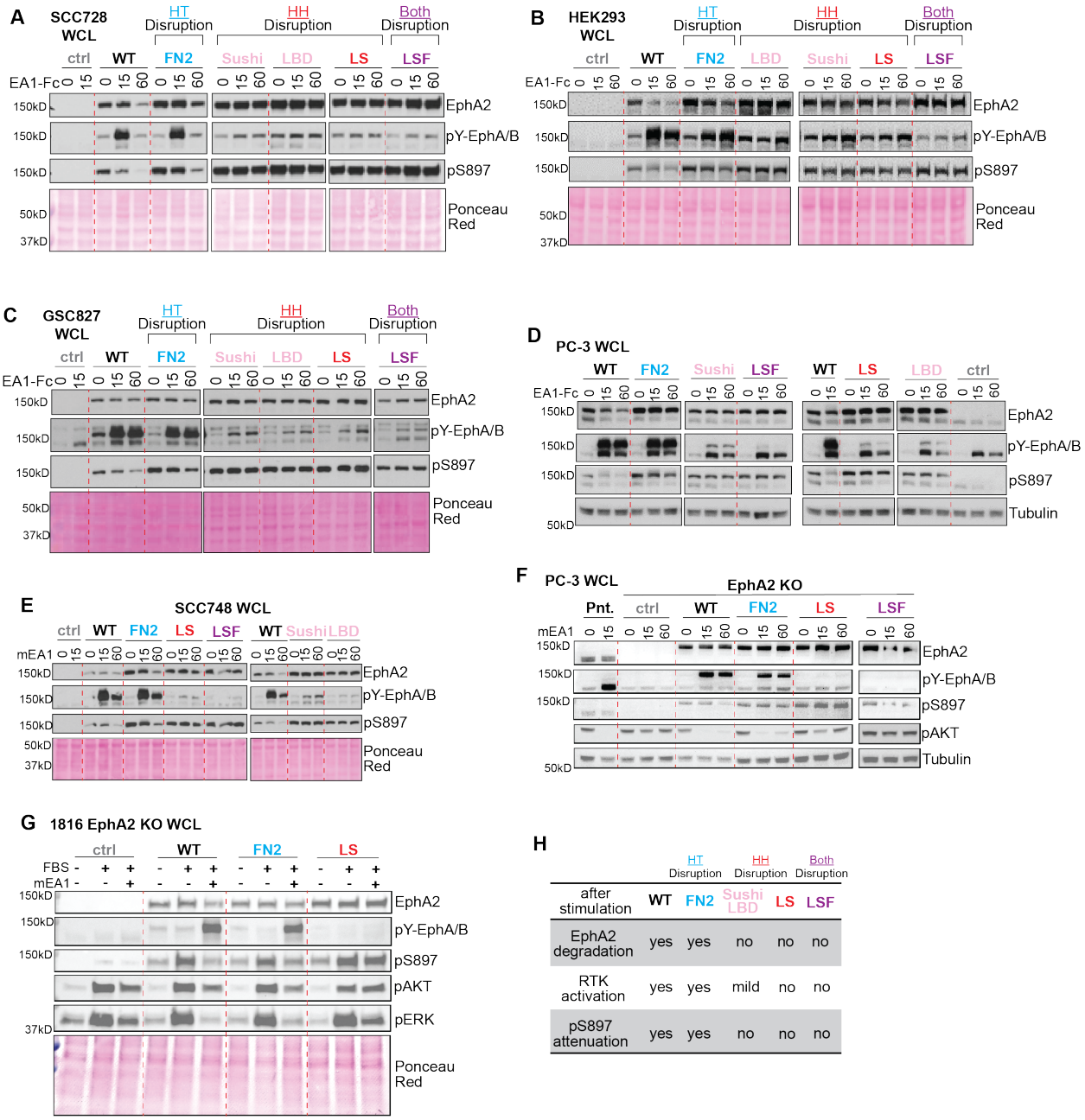

H

after stimulation	WT	FN2	Sushi LBD	LS	LSF
	HT Disruption		HH Disruption		Both Disruption
EphA2 degradation	yes	yes	no	no	no
RTK activation	yes	yes	mild	no	no
pS897 attenuation	yes	yes	no	no	no

Figure S4 in supporting of Figure 3.
A, B, C, D, E, F) EphA2 constructs are expressed in SCC728 **(A)**, HEK293 **(B)**, GSC827 **(C)**, PC-3 **(D),** SCC748 **(E)** and PC-3 EphA2KO **(F)** and 1816 EphA2KO **(G)** cells. Cells are stimulated with 3 μg/mL EA1-Fc (**A-D**) or mEA1 (**E, F**) for 15 min and 60 min and lysed. Alternatively, cells were starved for 24 hours and then treated with 2% FBS plus 3 μg/mL mEA1 and lysed (**G**). Whole-cell lysates are subjected to immunoblot with the indicated antibodies. **H)** Summary of the results from immunoblots. A short version of SCC728 blots **(A)** is presented in **Figure 3**.

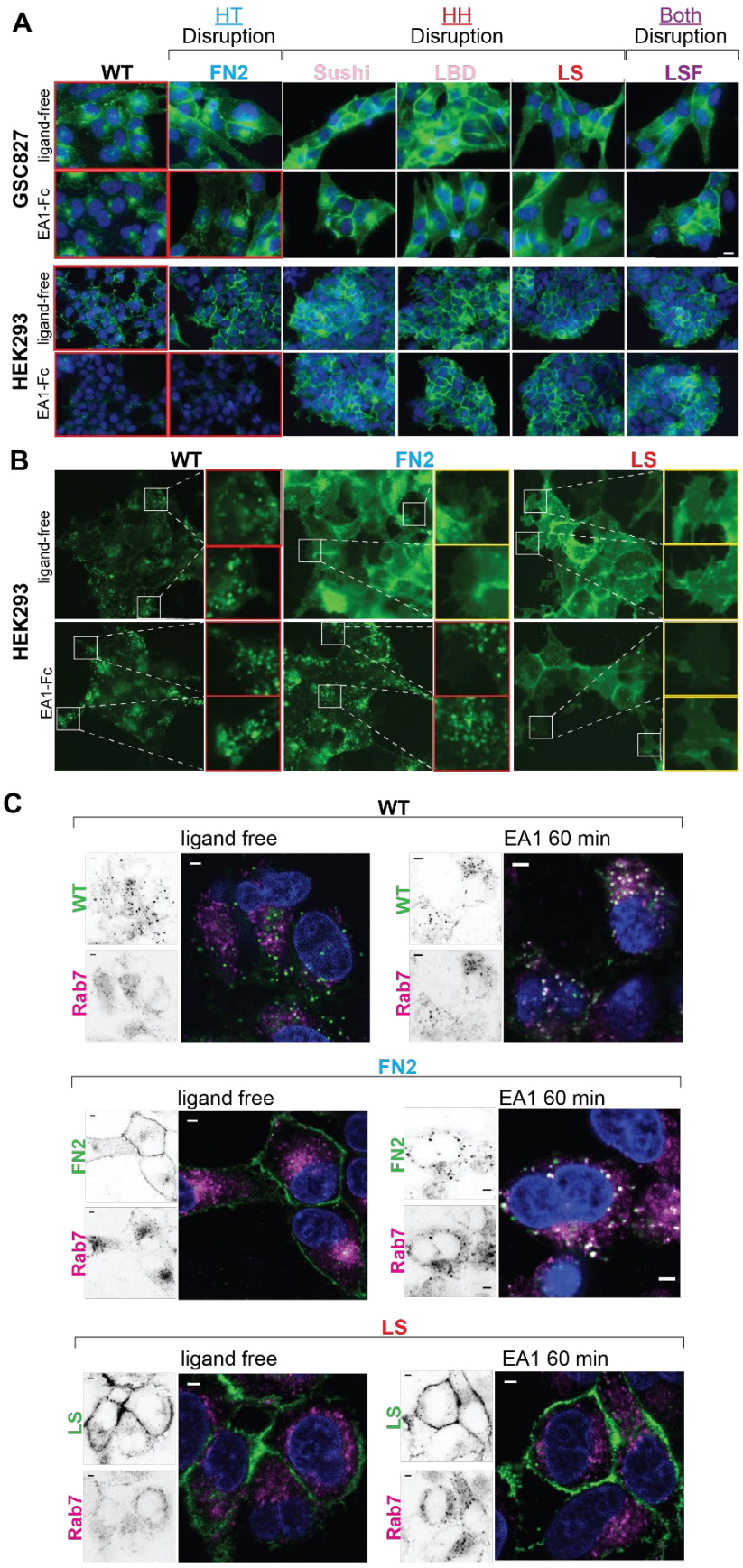
A
HT Disruption
HH Disruption
Both Disruption
WT
FN2
Sushi
LBD
LS
LSF
GSC827
HEK293
ligand-free
EA1-Fc
B
WT
FN2
LS
HEK293
ligand-free
EA1-Fc
C
WT
ligand free
EA1 60 min
WT
Rab7
FN2
ligand free
EA1 60 min
FN2
Rab7
LS
ligand free
EA1 60 min
LS
Rab7

Figure S5 in supporting of Figure 3.

A) Epi-fluorescence images of GSC827 (top) and HEK293 (bottom) cells with the expression of EphA2 constructs at ligand-free and EA1-stimulated states. Punctuated features and less membrane retention of EphA2 are observed with WT, and FN2 at stimulated state (highlighted with red box), suggesting active endocytosis the receptors. **B)** Epi-fluorescence images of HEK293 with different EphA2 localization patterns. **C)** Confocal images of GSC827 cells expressing EphA2-GFP (green) and stained for Rab7 (magenta). The nucleus was stained with DAPI (blue). Separated images of EphA2 constructs and Rab7 proteins are shown in inverted format. Merged images of the cells are shown in colors. White features indicate colocalization of EphA2 and Rab7. All scale bars are 5 μm.

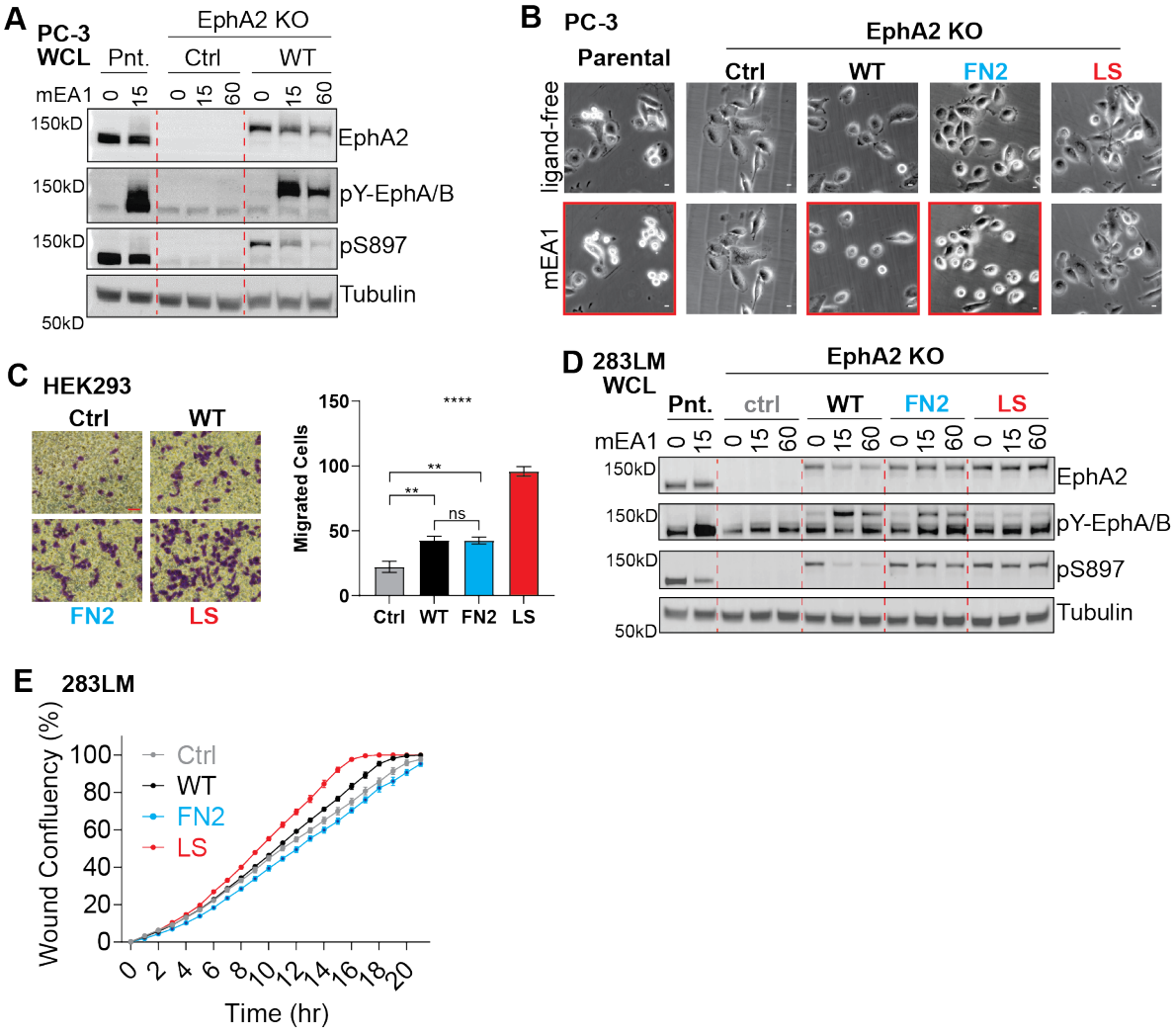
A
PC-3
WCL
Pnt.
EphA2 KO
Ctrl
WT
mEA1
0
15
0
15
60
0
15
60
150kD
EphA2
150kD
pY-EphA/B
150kD
pS897
Tubulin
50kD
B
PC-3
Parental
EphA2 KO
Ctrl
WT
FN2
LS
ligand-free
mEA1
C
HEK293
Ctrl
WT
FN2
LS
Migrated Cells
150
100
50
0
****
**
**
ns
Ctrl
WT
FN2
LS
D
283LM
WCL
EphA2 KO
Pnt.
ctrl
WT
FN2
LS
mEA1
0
15
0
15
60
0
15
60
0
15
60
0
15
60
150kD
EphA2
150kD
pY-EphA/B
150kD
pS897
Tubulin
50kD
E
283LM
Wound Confluency (%)
100
80
60
40
20
0
Ctrl
WT
FN2
LS
0
2
4
6
8
10
12
14
16
18
20
Time (hr)

Figure S6 in supporting of Figure 4.

A) PC-3 cells are stimulated with 3 μg/mL mEA1 for 15 min and 60 min, and lysed. Whole-cell lysates are subjected to immunoblot with the indicated antibodies. **B)** Example images of PC-3 EphA2KO cells expressing EphA2 constructs responding to mEA1 stimulation. Images are acquired at 0 and 10min after ligand stimulation. Cell membrane retraction is observed with WT and FN2 expressing cells (highlighted with red boxes), but not with LS expressing cells. Scale bars: 20 μm. **C)** *Left:* Example images of HEK293 cells expressing EphA2 constructs in trans-well migration assay. Images are acquired after 4h of incubation. Migrated cells on the bottom of trans-well membranes are stained with crystal violet and counted. Scale bar: 10 μm. *Right:* Number of migrated cells are summarized in bar graphs to report the mean value. The error bars represent SEM. (One-way ANOVA test. ****: $p < 0.0001$; **: $p < 0.01$; ns: not significant) **D)** EphA2 constructs are expressed in 283LM cells are stimulated with 3 μg/mL mEA1 for 15 min and 60 min, and lysed. Whole-cell lysates are subjected to immunoblot with the indicated antibodies. **E)** Time course of the wounding healing assay of 283LM cells.

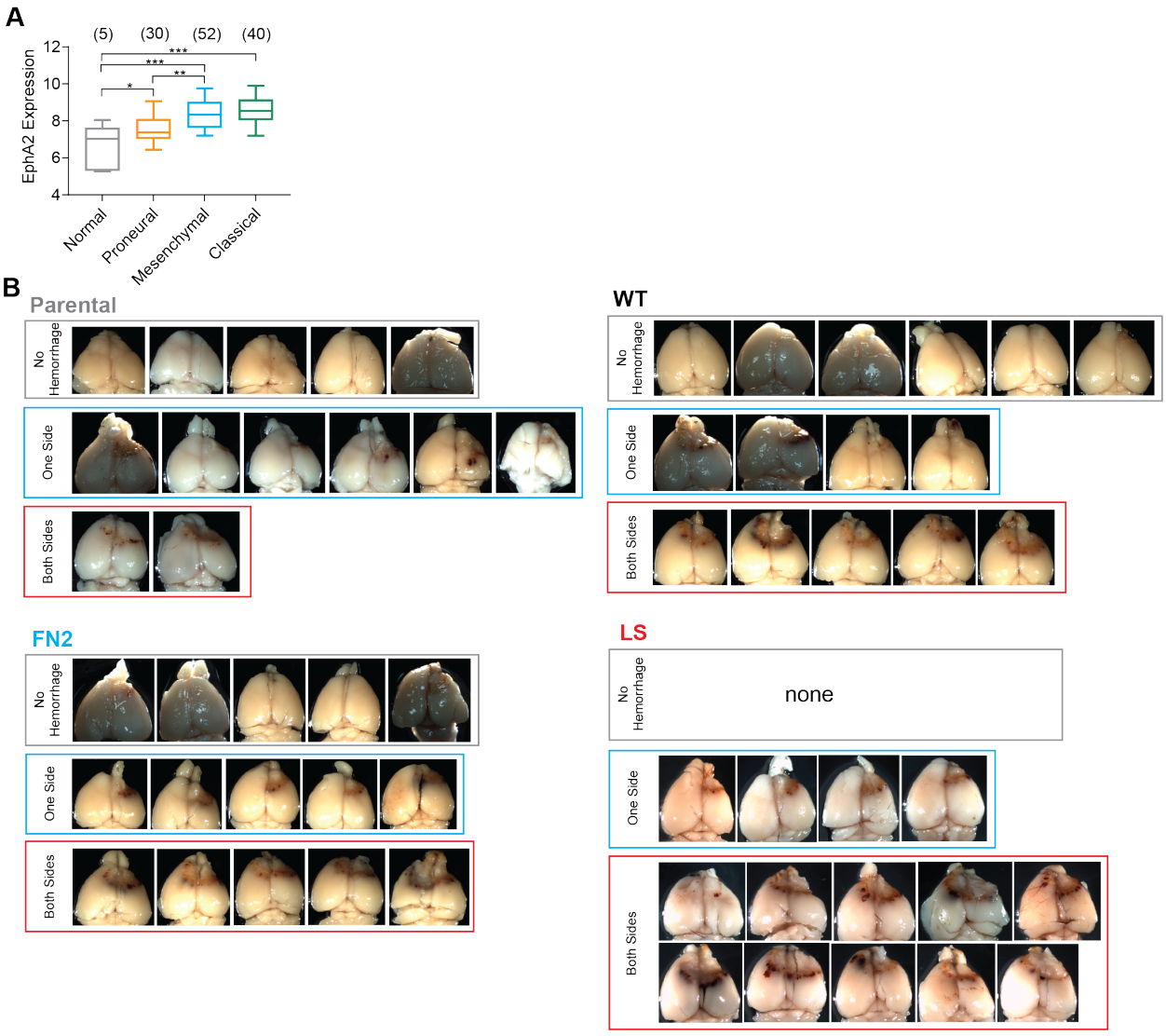
A
(5)
(30)
(52)
(40)
***
***
**
*
EphA2 Expression
12
10
8
6
4
Normal
Proneural
Mesenchymal
Classical
B
Parental
No Hemorrhage
One Side
Both Sides
WT
No Hemorrhage
One Side
Both Sides
FN2
No Hemorrhage
One Side
Both Sides
LS
No Hemorrhage
none
One Side
Both Sides

Figure S7 in supporting of Figure 4.

A) Expression levels of EphA2 in different types of brain tumor. Data acquired from TCGA. The boxes represent third quartile, median and first quartile and the whiskers indicate 10-90th percentile. The sample number used were reported on top of the box-whisker plots. (One-way ANOVA test. ***: $p < 0.001$; **: $p < 0.01$; *: $p < 0.05$) **B)** Images of all the brain samples from the gliomagenesis experiment. The samples are divided into groups according to the patterns of the hemorrhage. The brains injected with LS expressing cells show most severe hemorrhages.

EphA2	ligand-free	monomeric ephrin-A1	ephrin-A1-Fc	f_c	D ($\mu m^2/s$)	GFP lifetime (ns)	Anisotropy
WT	+			0.24	0.33	2.13	0.025
WT		+		0.48	0.15	2.05	
WT			+	0.52	0.13	2.03	
FN2	+			0.15	0.53	2.17	0.014
FN2		+		0.37	0.24	2.09	
FN2			+	0.48	0.2	2.07	
LBD	+			0.15	0.54	2.15	
LBD		+		0.14	0.62	2.15	
LBD			+	0.3	0.3	2.12	
Sushi	+			0.12	0.59	2.18	
Sushi		+		0.25	0.43	2.18	
Sushi			+	0.3	0.29	2.17	
LS	+			0.11	0.6	2.14	0.042
LS		+		0.06	0.74	2.15	
LS			+	0.27	0.33	2.11	
LSF	+			0.03	0.82	2.16	0.096
LSF		+		0.03	0.62	2.19	
LSF			+	0.18	0.36	2.18	
FN1	+			0.25	0.35	2.17	
FN1		+		0.5	0.15	2.02	
FN1			+	0.55	0.1	2.03	

Table S1.
Summary of multiplex reads from PIE-FCCS and Anisotropy measurements.

Movie S1.

Example time lapse images of HEK293 cells expressing WT in response to EA1 stimulation. Significant cell rounding was observed.

Movie S2.

Example time lapse images of HEK293 cells expressing FN2 in response to EA1 stimulation. Significant cell rounding was observed.

Movie S3.

Example time lapse images of HEK293 cells expressing LS in response to EA1 stimulation. No cell rounding was observed.

Movie S4.

Example time lapse images of HEK293 cells expressing pBabe vector in response to EA1 stimulation. No cell rounding was observed.

References and Notes

1. A. Kania, R. Klein, Mechanisms of ephrin-Eph signalling in development, physiology and disease. *Nat. Rev. Mol. Cell Biol.* **17**, 240–256 (2016). doi:10.1038/nrm.2015.16 Medline

2. D. G. Wilkinson, Multiple roles of EPH receptors and ephrins in neural development. *Nat. Rev. Neurosci.* **2**, 155–164 (2001). doi:10.1038/35058515 Medline

3. E. B. Pasquale, Eph-ephrin bidirectional signaling in physiology and disease. *Cell* **133**, 38–52 (2008). doi:10.1016/j.cell.2008.03.011 Medline

4. J. Wykosky, W. Debinski, The EphA2 receptor and ephrinA1 ligand in solid tumors: Function and therapeutic targeting. *Mol. Cancer Res.* **6**, 1795–1806 (2008). doi:10.1158/1541-7786.MCR-08-0244 Medline

5. E. B. Pasquale, Eph receptors and ephrins in cancer: Bidirectional signalling and beyond. *Nat. Rev. Cancer* **10**, 165–180 (2010). doi:10.1038/nrc2806 Medline

6. R. C. Ireton, J. Chen, EphA2 receptor tyrosine kinase as a promising target for cancer therapeutics. *Curr. Cancer Drug Targets* **5**, 149–157 (2005). doi:10.2174/1568009053765780 Medline

7. H. Miao, B. Wang, Eph/ephrin signaling in epithelial development and homeostasis. *Int. J. Biochem. Cell Biol.* **41**, 762–770 (2009). doi:10.1016/j.biocel.2008.07.019 Medline

8. F. Al-Ejeh, C. Offenhäuser, Y. C. Lim, B. W. Stringer, B. W. Day, A. W. Boyd, Eph family co-expression patterns define unique clusters predictive of cancer phenotype. *Growth Factors* **32**, 254–264 (2014). doi:10.3109/08977194.2014.984807 Medline

9. M. Macrae, R. M. Neve, P. Rodriguez-Viciana, C. Haqq, J. Yeh, C. Chen, J. W. Gray, F. McCormick, A conditional feedback loop regulates Ras activity through EphA2. *Cancer Cell* **8**, 111–118 (2005). doi:10.1016/j.ccr.2005.07.005 Medline

10. H. Miao, B.-R. Wei, D. M. Peehl, Q. Li, T. Alexandrou, J. R. Schelling, J. S. Rhim, J. R. Sedor, E. Burnett, B. Wang, Activation of EphA receptor tyrosine kinase inhibits the Ras/MAPK pathway. *Nat. Cell Biol.* **3**, 527–530 (2001). doi:10.1038/35074604 Medline

11. N. Y. Yang, C. Fernandez, M. Richter, Z. Xiao, F. Valencia, D. A. Tice, E. B. Pasquale, Crosstalk of the EphA2 receptor with a serine/threonine phosphatase suppresses the Akt-mTORC1 pathway in cancer cells. *Cell. Signal.* **23**, 201–212 (2011). doi:10.1016/j.cellsig.2010.09.004 Medline

12. H. Miao, E. Burnett, M. Kinch, E. Simon, B. Wang, Activation of EphA2 kinase suppresses integrin function and causes focal-adhesion-kinase dephosphorylation. *Nat. Cell Biol.* **2**, 62–69 (2000). doi:10.1038/35000008 Medline

13. H. Miao, D.-Q. Li, A. Mukherjee, H. Guo, A. Petty, J. Cutter, J. P. Basilion, J. Sedor, J. Wu, D. Danielpour, A. E. Sloan, M. L. Cohen, B. Wang, EphA2 mediates ligand-dependent inhibition and ligand-independent promotion of cell migration and invasion via a reciprocal regulatory loop with Akt. *Cancer Cell* **16**, 9–20 (2009). doi:10.1016/j.ccr.2009.04.009 Medline

14. W. Stallaert, Y. Brüggemann, O. Sabet, L. Baak, M. Gattiglio, P. I. H. Bastiaens, Contact inhibitory Eph signaling suppresses EGF-promoted cell migration by decoupling EGFR

activity from vesicular recycling. *Sci. Signal.* **11**, eaat0114 (2018). doi:10.1126/scisignal.aat0114 Medline

15. H. Guo, H. Miao, L. Gerber, J. Singh, M. F. Denning, A. C. Gilliam, B. Wang, Disruption of EphA2 receptor tyrosine kinase leads to increased susceptibility to carcinogenesis in mouse skin. *Cancer Res.* **66**, 7050–7058 (2006). doi:10.1158/0008-5472.CAN-06-0004 Medline

16. A. Barquilla, I. Lamberto, R. Noberini, S. Heynen-Genel, L. M. Brill, E. B. Pasquale, Protein kinase A can block EphA2 receptor-mediated cell repulsion by increasing EphA2 S897 phosphorylation. *Mol. Biol. Cell* **27**, 2757–2770 (2016). doi:10.1091/mbc.e16-01-0048 Medline

17. H. Miao, N. W. Gale, H. Guo, J. Qian, A. Petty, J. Kaspar, A. J. Murphy, D. M. Valenzuela, G. Yancopoulos, D. Hambardzumyan, J. D. Lathia, J. N. Rich, J. Lee, B. Wang, EphA2 promotes infiltrative invasion of glioma stem cells in vivo through cross-talk with Akt and regulates stem cell properties. *Oncogene* **34**, 558–567 (2015). doi:10.1038/onc.2013.590 Medline

18. C. Volz, S. Breid, C. Selenz, A. Zaplatina, K. Golfmann, L. Meder, F. Dietlein, S. Borchmann, S. Chatterjee, M. Siobal, J. Schöttle, A. Florin, M. Koker, M. Nill, L. Ozretić, N. Uhlenbrock, S. Smith, R. Büttner, H. Miao, B. Wang, H. C. Reinhardt, D. Rauh, M. Hallek, A. Acker-Palmer, L. C. Heukamp, R. T. Ullrich, Inhibition of tumor VEGFR2 induces serine 897 EphA2-dependent tumor cell invasion and metastasis in NSCLC. *Cell Rep.* **31**, 107568 (2020). doi:10.1016/j.celrep.2020.107568 Medline

19. A. Azimi, R. Tuominen, F. Costa Svedman, S. Caramuta, M. Pernemalm, M. Frostvik Stolt, L. Kanter, P. Kharaziha, J. Lehtiö, C. Hertzman Johansson, V. Höiom, J. Hansson, S. Egyhazi Brage, Silencing FLI or targeting CD13/ANPEP lead to dephosphorylation of EPHA2, a mediator of BRAF inhibitor resistance, and induce growth arrest or apoptosis in melanoma cells. *Cell Death Dis.* **8**, e3029 (2017). doi:10.1038/cddis.2017.406 Medline

20. K. H. Paraiso, M. Das Thakur, B. Fang, J. M. Koomen, I. V. Fedorenko, J. K. John, H. Tsao, K. T. Flaherty, V. K. Sondak, J. L. Messina, E. B. Pasquale, A. Villagra, U. N. Rao, J. M. Kirkwood, F. Meier, S. Sloot, G. T. Gibney, D. Stuart, H. Tawbi, K. S. M. Smalley, Ligand-independent EPHA2 signaling drives the adoption of a targeted therapy-mediated metastatic melanoma phenotype. *Cancer Discov.* **5**, 264–273 (2015). doi:10.1158/2159-8290.CD-14-0293 Medline

21. L. Moyano-Galceran, E. A. Pietilä, S. P. Turunen, S. Corvigno, E. Hjerpe, D. Bulanova, U. Joneborg, T. Alkasalias, Y. Miki, M. Yashiro, A. Chernenko, J. Jukonen, M. Singh, H. Dahlstrand, J. W. Carlson, K. Lehti, Adaptive RSK-EphA2-GPRC5A signaling switch triggers chemotherapy resistance in ovarian cancer. *EMBO Mol. Med.* **12**, e11177 (2020). doi:10.15252/emmm.201911177 Medline

22. A. Sachdeva, C. A. Hart, K. Kim, T. Tawadros, P. Oliveira, J. Shanks, M. Brown, N. Clarke, Non-canonical EphA2 activation underpins PTEN-mediated metastatic migration and poor clinical outcome in prostate cancer. *Br. J. Cancer* **127**, 1254–1262 (2022). doi:10.1038/s41416-022-01914-3 Medline

23. C. Zhang, I. Smalley, M. F. Emmons, R. Sharma, V. Izumi, J. Messina, J. M. Koomen, E. B. Pasquale, P. A. Forsyth, K. S. M. Smalley, Non-canonical EphA2 signaling is a driver of tumor-endothelial cell interactions and metastatic dissemination in BRAF inhibitor–

resistant melanoma. *J. Invest. Dermatol.* **141**, 840–851.e4 (2020). doi:10.1016/j.jid.2020.08.012 Medline

24. V. M. Youngblood, L. C. Kim, D. N. Edwards, Y. Hwang, P. R. Santapuram, S. M. Stirdivant, P. Lu, F. Ye, D. M. Brantley-Sieders, J. Chen, The Ephrin-A1/EPHA2 signaling axis regulates glutamine metabolism in HER2-positive breast cancer. *Cancer Res.* **76**, 1825–1836 (2016). doi:10.1158/0008-5472.CAN-15-0847 Medline

25. L. Fattet, H.-Y. Jung, M. W. Matsumoto, B. E. Aubol, A. Kumar, J. A. Adams, A. C. Chen, R. L. Sah, A. J. Engler, E. B. Pasquale, J. Yang, Matrix rigidity controls epithelial-mesenchymal plasticity and tumor metastasis via a mechanoresponsive EPHA2/LYN complex. *Dev. Cell* **54**, 302–316.e7 (2020). doi:10.1016/j.devcel.2020.05.031 Medline

26. D. Mitra, S. Bhattacharyya, N. Alam, S. Sen, S. Mitra, S. Mandal, S. Vignesh, B. Majumder, N. Murmu, Phosphorylation of EphA2 receptor and vasculogenic mimicry is an indicator of poor prognosis in invasive carcinoma of the breast. *Breast Cancer Res. Treat.* **179**, 359–370 (2020). doi:10.1007/s10549-019-05482-8 Medline

27. J. P. Himanen, D. B. Nikolov, Eph signaling: A structural view. *Trends Neurosci.* **26**, 46–51 (2003). doi:10.1016/S0166-2236(02)00005-X Medline

28. E. Seiradake, K. Harlos, G. Sutton, A. R. Aricescu, E. Y. Jones, An extracellular steric seeding mechanism for Eph-ephrin signaling platform assembly. *Nat. Struct. Mol. Biol.* **17**, 398–402 (2010). doi:10.1038/nsmb.1782 Medline

29. J. P. Himanen, L. Yermekbayeva, P. W. Janes, J. R. Walker, K. Xu, L. Atapattu, K. R. Rajashankar, A. Mensinga, M. Lackmann, D. B. Nikolov, S. Dhe-Paganon, Architecture of Eph receptor clusters. *Proc. Natl. Acad. Sci. U.S.A.* **107**, 10860–10865 (2010). doi:10.1073/pnas.1004148107 Medline

30. K. Salaita, P. M. Nair, R. S. Petit, R. M. Neve, D. Das, J. W. Gray, J. T. Groves, Restriction of receptor movement alters cellular response: Physical force sensing by EphA2. *Science* **327**, 1380–1385 (2010). doi:10.1126/science.1181729 Medline

31. O. Sabet, R. Stockert, G. Xouri, Y. Brüggemann, A. Stanoev, P. I. H. Bastiaens, Ubiquitination switches EphA2 vesicular traffic from a continuous safeguard to a finite signalling mode. *Nat. Commun.* **6**, 8047 (2015). doi:10.1038/ncomms9047 Medline

32. D. R. Singh, F. Ahmed, C. King, N. Gupta, M. Salotto, E. B. Pasquale, K. Hristova, EphA2 receptor unliganded dimers suppress EphA2 pro-tumorigenic signaling. *J. Biol. Chem.* **290**, 27271–27279 (2015). doi:10.1074/jbc.M115.676866 Medline

33. K. Bacia, P. Schwille, Practical guidelines for dual-color fluorescence cross-correlation spectroscopy. *Nat. Protoc.* **2**, 2842–2856 (2007). doi:10.1038/nprot.2007.410 Medline

34. B. K. Müller, E. Zaychikov, C. Bräuchle, D. C. Lamb, Pulsed interleaved excitation. *Biophys. J.* **89**, 3508–3522 (2005). doi:10.1529/biophysj.105.064766 Medline

35. S. Christie, X. Shi, A. W. Smith, Resolving membrane protein-protein interactions in live cells with pulsed interleaved excitation fluorescence cross-correlation spectroscopy. *Acc. Chem. Res.* **53**, 792–799 (2020). doi:10.1021/acs.accounts.9b00625 Medline

36. M. J. Kaliszewski, X. Shi, Y. Hou, R. Lingerak, S. Kim, P. Mallory, A. W. Smith, Quantifying membrane protein oligomerization with fluorescence cross-correlation

spectroscopy. *Methods* **140–141**, 40–51 (2018). doi:10.1016/j.ymeth.2018.02.002 Medline

37. N. F. Endres, R. Das, A. W. Smith, A. Arkhipov, E. Kovacs, Y. Huang, J. G. Pelton, Y. Shan, D. E. Shaw, D. E. Wemmer, J. T. Groves, J. Kuriyan, Conformational coupling across the plasma membrane in activation of the EGF receptor. *Cell* **152**, 543–556 (2013). doi:10.1016/j.cell.2012.12.032 Medline

38. K. Xu, D. Tzvetkova-Robev, Y. Xu, Y. Goldgur, Y.-P. Chan, J. P. Himanen, D. B. Nikolov, Insights into Eph receptor tyrosine kinase activation from crystal structures of the EphA4 ectodomain and its complex with ephrin-A5. *Proc. Natl. Acad. Sci. U.S.A.* **110**, 14634–14639 (2013). doi:10.1073/pnas.1311000110 Medline

39. S. Davis, N. W. Gale, T. H. Aldrich, P. C. Maisonpierre, V. Lhotak, T. Pawson, M. Goldfarb, G. D. Yancopoulos, Ligands for EPH-related receptor tyrosine kinases that require membrane attachment or clustering for activity. *Science* **266**, 816–819 (1994). doi:10.1126/science.7973638 Medline

40. J. Wykosky, E. Palma, D. M. Gibo, S. Ringler, C. P. Turner, W. Debinski, Soluble monomeric EphrinA1 is released from tumor cells and is a functional ligand for the EphA2 receptor. *Oncogene* **27**, 7260–7273 (2008). doi:10.1038/onc.2008.328 Medline

41. Q. Xu, W. C. Lin, R. S. Petit, J. T. Groves, EphA2 receptor activation by monomeric Ephrin-A1 on supported membranes. *Biophys. J.* **101**, 2731–2739 (2011). doi:10.1016/j.bpj.2011.10.039 Medline

42. D. B. Nikolov, K. Xu, J. P. Himanen, Homotypic receptor-receptor interactions regulating Eph signaling. *Cell Adh. Migr.* **8**, 360–365 (2014). doi:10.4161/19336918.2014.971684 Medline

43. E. B. Pasquale, Eph receptor signalling casts a wide net on cell behaviour. *Nat. Rev. Mol. Cell Biol.* **6**, 462–475 (2005). doi:10.1038/nrm1662 Medline

44. J. Schlessinger, Receptor tyrosine kinases: Legacy of the first two decades. *Cold Spring Harb. Perspect. Biol.* **6**, a008912 (2014). doi:10.1101/cshperspect.a008912 Medline

45. N. F. Endres, T. Barros, A. J. Cantor, J. Kuriyan, Emerging concepts in the regulation of the EGF receptor and other receptor tyrosine kinases. *Trends Biochem. Sci.* **39**, 437–446 (2014). doi:10.1016/j.tibs.2014.08.001 Medline

46. M. Miaczynska, Effects of membrane trafficking on signaling by receptor tyrosine kinases. *Cold Spring Harb. Perspect. Biol.* **5**, a009035 (2013). doi:10.1101/cshperspect.a009035 Medline

47. M. E. Pitulescu, R. H. Adams, Eph/ephrin molecules—A hub for signaling and endocytosis. *Genes Dev.* **24**, 2480–2492 (2010). doi:10.1101/gad.1973910 Medline

48. P. Boissier, J. Chen, U. Huynh-Do, EphA2 signaling following endocytosis: Role of Tiam1. *Traffic* **14**, 1255–1271 (2013). doi:10.1111/tra.12123 Medline

49. E. Binda, A. Visioli, F. Giani, G. Lamorte, M. Copetti, K. L. Pitter, J. T. Huse, L. Cajola, N. Zanetti, F. DiMeco, L. De Filippis, A. Mangiola, G. Maira, C. Anile, P. De Bonis, B. A. Reynolds, E. B. Pasquale, A. L. Vescovi, The EphA2 receptor drives self-renewal and tumorigenicity in stem-like tumor-propagating cells from human glioblastomas. *Cancer Cell* **22**, 765–780 (2012). doi:10.1016/j.ccr.2012.11.005 Medline

50. K. M. Reilly, D. A. Loisel, R. T. Bronson, M. E. McLaughlin, T. Jacks, Nf1;Trp53 mutant mice develop glioblastoma with evidence of strain-specific effects. *Nat. Genet.* **26**, 109–113 (2000). doi:10.1038/79075 Medline

51. D. B. Gürsel, Y. S. Connell-Albert, R. G. Tuskan, T. Anastassiadis, J. C. Walrath, J. J. Hawes, J. C. Amlin-Van Schaick, K. M. Reilly, Control of proliferation in astrocytoma cells by the receptor tyrosine kinase/PI3K/AKT signaling axis and the use of PI-103 and TCN as potential anti-astrocytoma therapies. *Neuro-oncol.* **13**, 610–621 (2011). doi:10.1093/neuonc/nor035 Medline

52. Y. Pan, L. J. Smithson, Y. Ma, D. Hambardzumyan, D. H. Gutmann, Ccl5 establishes an autocrine high-grade glioma growth regulatory circuit critical for mesenchymal glioblastoma survival. *Oncotarget* **8**, 32977–32989 (2017). doi:10.18632/oncotarget.16516 Medline

53. Z. Chen, D. Oh, K. H. Biswas, C.-H. Yu, R. Zaidel-Bar, J. T. Groves, Spatially modulated ephrinA1:EphA2 signaling increases local contractility and global focal adhesion dynamics to promote cell motility. *Proc. Natl. Acad. Sci. U.S.A.* **115**, E5696–E5705 (2018). doi:10.1073/pnas.1719961115 Medline

54. B. T. Bajar, E. S. Wang, S. Zhang, M. Z. Lin, J. Chu, a guide to fluorescent protein FRET pairs. *Sensors* **16**, 1488 (2016). doi:10.3390/s16091488 Medline

55. F. Carafoli, E. Hohenester, Collagen recognition and transmembrane signalling by discoidin domain receptors. *Biochim. Biophys. Acta* **1834**, 2187–2194 (2013). doi:10.1016/j.bbapap.2012.10.014 Medline

56. J. P. Himanen, Y. Goldgur, H. Miao, E. Myshkin, H. Guo, M. Buck, M. Nguyen, K. R. Rajashankar, B. Wang, D. B. Nikolov, Ligand recognition by A-class Eph receptors: Crystal structures of the EphA2 ligand-binding domain and the EphA2/ephrin-A1 complex. *EMBO Rep.* **10**, 722–728 (2009). doi:10.1038/embor.2009.91 Medline

57. X. Shi, V. Hapiak, J. Zheng, J. Muller-Greven, D. Bowman, R. Lingerak, M. Buck, B.-C. Wang, A. W. Smith, A role of the SAM domain in EphA2 receptor activation. *Sci. Rep.* **7**, 45084 (2017). doi:10.1038/srep45084 Medline

58. J. Lee, S. Kotliarova, Y. Kotliarov, A. Li, Q. Su, N. M. Donin, S. Pastorino, B. W. Purow, N. Christopher, W. Zhang, J. K. Park, H. A. Fine, Tumor stem cells derived from glioblastomas cultured in bFGF and EGF more closely mirror the phenotype and genotype of primary tumors than do serum-cultured cell lines. *Cancer Cell* **9**, 391–403 (2006). doi:10.1016/j.ccr.2006.03.030 Medline

59. D. Orsal, C. Perret, J. M. Cabelguen, Comparison between ventral spinocerebellar and rubrospinal activities during locomotion in the cat. *Behav. Brain Res.* **28**, 159–162 (1988). doi:10.1016/0166-4328(88)90092-7 Medline

60. J. N. Weinstein, E. A. Collisson, G. B. Mills, K. R. M. Shaw, B. A. Ozenberger, K. Ellrott, I. Shmulevich, C. Sander, J. M. Stuart; Cancer Genome Atlas Research Network, The Cancer Genome Atlas Pan-Cancer analysis project. *Nat. Genet.* **45**, 1113–1120 (2013). doi:10.1038/ng.2764 Medline

61. C. W. Brennan, R. G. W. Verhaak, A. McKenna, B. Campos, H. Noushmehr, S. R. Salama, S. Zheng, D. Chakravarty, J. Z. Sanborn, S. H. Berman, R. Beroukhim, B. Bernard, C.-J. Wu, G. Genovese, I. Shmulevich, J. Barnholtz-Sloan, L. Zou, R. Vegesna, S. A. Shukla,

G. Ciriello, W. K. Yung, W. Zhang, C. Sougnez, T. Mikkelsen, K. Aldape, D. D. Bigner, E. G. Van Meir, M. Prados, A. Sloan, K. L. Black, J. Eschbacher, G. Finocchiaro, W. Friedman, D. W. Andrews, A. Guha, M. Iacocca, B. P. O'Neill, G. Foltz, J. Myers, D. J. Weisenberger, R. Penny, R. Kucherlapati, C. M. Perou, D. N. Hayes, R. Gibbs, M. Marra, G. B. Mills, E. Lander, P. Spellman, R. Wilson, C. Sander, J. Weinstein, M. Meyerson, S. Gabriel, P. W. Laird, D. Haussler, G. Getz, L. Chin; TCGA Research Network, The somatic genomic landscape of glioblastoma. *Cell* **155**, 462–477 (2013). doi:10.1016/j.cell.2013.09.034 Medline

62. M. Erdelyi, J. Simon, E. A. Barnard, C. F. Kaminski, Analyzing receptor assemblies in the cell membrane using fluorescence anisotropy imaging with TIRF microscopy. *PLOS ONE* **9**, e100526 (2014). doi:10.1371/journal.pone.0100526 Medline

63. S. Ghosh, S. Saha, D. Goswami, S. Bilgrami, S. Mayor, in vol. 505 of *Methods in Enzymology*, P. M. Conn, Ed. (Academic Press, 2012), pp. 291–327.

64. J. K. Leman, B. D. Weitzner, S. M. Lewis, J. Adolf-Bryfogle, N. Alam, R. F. Alford, M. Aprahamian, D. Baker, K. A. Barlow, P. Barth, B. Basanta, B. J. Bender, K. Blacklock, J. Bonet, S. E. Boyken, P. Bradley, C. Bystroff, P. Conway, S. Cooper, B. E. Correia, B. Coventry, R. Das, R. M. De Jong, F. DiMaio, L. Dsilva, R. Dunbrack, A. S. Ford, B. Frenz, D. Y. Fu, C. Geniesse, L. Goldschmidt, R. Gowthaman, J. J. Gray, D. Gront, S. Guffy, S. Horowitz, P.-S. Huang, T. Huber, T. M. Jacobs, J. R. Jeliazkov, D. K. Johnson, K. Kappel, J. Karanicolas, H. Khakzad, K. R. Khar, S. D. Khare, F. Khatib, A. Khramushin, I. C. King, R. Kleffner, B. Koepnick, T. Kortemme, G. Kuenze, B. Kuhlman, D. Kuroda, J. W. Labonte, J. K. Lai, G. Lapidoth, A. Leaver-Fay, S. Lindert, T. Linsky, N. London, J. H. Lubin, S. Lyskov, J. Maguire, L. Malmström, E. Marcos, O. Marcu, N. A. Marze, J. Meiler, R. Moretti, V. K. Mulligan, S. Nerli, C. Norn, S. Ó'Conchúir, N. Ollikainen, S. Ovchinnikov, M. S. Pacella, X. Pan, H. Park, R. E. Pavlovicz, M. Pethe, B. G. Pierce, K. B. Pilla, B. Raveh, P. D. Renfrew, S. S. R. Burman, A. Rubenstein, M. F. Sauer, A. Scheck, W. Schief, O. Schueler-Furman, Y. Sedan, A. M. Sevy, N. G. Sgourakis, L. Shi, J. B. Siegel, D.-A. Silva, S. Smith, Y. Song, A. Stein, M. Szegedy, F. D. Teets, S. B. Thyme, R. Y.-R. Wang, A. Watkins, L. Zimmerman, R. Bonneau, Macromolecular modeling and design in Rosetta: Recent methods and frameworks. *Nat. Methods* **17**, 665–680 (2020). doi:10.1038/s41592-020-0848-2 Medline

65. Y. Song, F. DiMaio, R. Y.-R. Wang, D. Kim, C. Miles, T. Brunette, J. Thompson, D. Baker, High-resolution comparative modeling with RosettaCM. *Structure* **21**, 1735–1742 (2013). doi:10.1016/j.str.2013.08.005 Medline

66. R. F. Alford, A. Leaver-Fay, J. R. Jeliazkov, M. J. O'Meara, F. P. DiMaio, H. Park, M. V. Shapovalov, P. D. Renfrew, V. K. Mulligan, K. Kappel, J. W. Labonte, M. S. Pacella, R. Bonneau, P. Bradley, R. L. Dunbrack Jr., R. Das, D. Baker, B. Kuhlman, T. Kortemme, J. J. Gray, The Rosetta All-Atom Energy Function for macromolecular modeling and design. *J. Chem. Theory Comput.* **13**, 3031–3048 (2017). doi:10.1021/acs.jctc.7b00125 Medline

67. B. Frenz, S. M. Lewis, I. King, F. DiMaio, H. Park, Y. Song, Prediction of protein mutational free energy: Benchmark and sampling improvements increase classification accuracy. *Front. Bioeng. Biotechnol.* **8**, 558247 (2020). doi:10.3389/fbioe.2020.558247 Medline

68. C. Tian, K. Kasavajhala, K. A. A. Belfon, L. Raguette, H. Huang, A. N. Migues, J. Bickel, Y.

Wang, J. Pincay, Q. Wu, C. Simmerling, ff19SB: Amino-acid-specific protein backbone parameters trained against quantum mechanics energy surfaces in solution. *J. Chem. Theory Comput.* **16**, 528–552 (2020). doi:10.1021/acs.jctc.9b00591 Medline

69. I. S. Joung, T. E. Cheatham III, Determination of alkali and halide monovalent ion parameters for use in explicitly solvated biomolecular simulations. *J. Phys. Chem. B* **112**, 9020–9041 (2008). doi:10.1021/jp8001614 Medline

70. C. W. Hopkins, S. Le Grand, R. C. Walker, A. E. Roitberg, Long-time-step molecular dynamics through hydrogen mass repartitioning. *J. Chem. Theory Comput.* **11**, 1864–1874 (2015). doi:10.1021/ct5010406 Medline

71. J.-P. Ryckaert, G. Ciccotti, H. J. C. Berendsen, Numerical integration of the cartesian equations of motion of a system with constraints: Molecular dynamics of n-alkanes. *J. Comput. Phys.* **23**, 327–341 (1977). doi:10.1016/0021-9991(77)90098-5

72. D. R. Roe, T. E. Cheatham III, PTRAJ and CPPTRAJ: Software for processing and analysis of molecular dynamics trajectory data. *J. Chem. Theory Comput.* **9**, 3084–3095 (2013). doi:10.1021/ct400341p Medline